Interaction of a planar shock wave and a water droplet embedded with a vapour cavity

Yu Liang[1,2], Yazhong Jiang[1]†, Chih-Yung Wen[1]‡ and Yao Liu[1]

[1]Department of Mechanical Engineering and Interdisplinary Division of Aeronautical and Aviation Engineering, The Hong Kong Polytechnic University, Kowloon, Hong Kong, China
[2]Advanced Propulsion Laboratory, Department of Modern Mechanics, University of Science and Technology of China, Hefei 230026, China

(Received ? ; revised ? ; accepted ?. - To be entered by editorial office)

The interaction of a shock wave and a water droplet embedded with a vapour cavity is experimentally investigated in a shock tube for the first time. The vapour cavity inside the droplet is generated by decreasing the surrounding pressure to the saturation pressure, and an equilibrium between the liquid phase and the gas phase is obtained inside the droplet. Direct high-speed photography is adopted to capture the evolution of both the droplet and the vapour cavity. The formation of a transverse jet inside the droplet during the cavity-collapse stage is clearly observed. Soon afterward, at the downstream pole of the droplet, a water jet penetrating into the surrounding air is observed during the cavity-expansion stage. The evolution of the droplet is strongly influenced by the evolution of the vapour cavity. The phase change process plays an important role in vapour cavity evolution. The effects of the relative size and eccentricity of the cavity on the movement and deformation of the droplet are presented quantitatively.

Key words: Authors should not enter keywords on the manuscript

1. Introduction

The shock-droplet interaction is a fundamental and challenging two-phase flow problem that occurs in many high-speed flow scenarios. Research on this problem has been performed for decades in aerospace and nuclear engineering communities due to its importance in industrial applications, such as the ablation management of space vehicles caused by rain droplet impingement during an atmosphere reentry, supersonic combustion in multiphase mixtures for scramjet engines, and damage evaluation and evacuation planning in the case of a nuclear plant explosion. The droplet-breakup process has attracted substantial attention, and comprehensive reviews can be found in Wierzba & Takayama (1988); Guildenbecher *et al.* (2009); Joseph *et al.* (1999) and Theofanous (2011).

Recently, the phenomenon that cavitation bubbles appear in a droplet was experimentally observed in shock-water-column interaction (Sembian *et al.* 2016) and droplet-solid-wall impingement (Field & Ogren 1989; Field *et al.* 2012), where rarefaction waves and tension waves respectively play important roles in the formation of the cavitation bubbles. Additionally, the numerical simulation in Kondo & Ando (2016) indicated that

† Email address for correspondence: yazhong.jiang@polyu.edu.hk
‡ Email address for correspondence: chihyung.wen@polyu.edu.hk

cavitation bubbles can be nucleated by the interaction of water-hammer shocks and droplet interfaces. In some industrial applications, it is possible that a liquid droplet is embedded with a gas cavity. A typical scenario is volatile perfluoropentane contained in the droplet used in ultrasound therapy (Shpak *et al.* 2016). Another example is related to the fuel droplet in scramjet engines. Because cavity collapse in liquid leads to cavitation erosion and surface damage (Philipp & Lauterborn 1998; Kodama & Tomita 2000; Brujan *et al.* 2002), it is believed that the evolution of the shocked gas cavity inside a droplet influences droplet deformation (Bhattacharya 2016). Recently, Xiang & Wang (2017) numerically investigated the interaction of a planar shock and a water column embedded with an air cavity. In this investigation, the effects of the shock intensities and the gas cavity sizes on the evolution of the droplet and the cavity were analysed qualitatively and quantitatively. Later, Wu *et al.* (2019) conducted numerical simulations to study the impingement of a cylindrical water column embedded with an air/vapour cavity on a rigid wall, and the interaction of the reflected water-hammer shock with the gas cavity was considered. In addition, the phase change process was considered in the numerical work of Wu *et al.* (2019), and the differences between the collapse of an air cavity and the collapse of a vapour cavity were analysed. However, the interaction of a shock wave and a droplet embedded with a gas cavity has not been experimentally investigated due to the challenge of generating such droplets. In addition, most previous studies have focused on cylindrical liquid columns, but spherical droplets are more common in nature.

In the present study, a water droplet embedded with a vapour cavity is generated by depressurization of the surrounding air (Liu *et al.* 2018). The size and position of the vapour cavity inside the droplet is uncontrollable. Nevertheless, satisfactory sphericity for the droplet and cavity can be achieved. Shock-tube experiments are conducted systematically, and direct high-speed photography is adopted to capture the deformations of both the droplet and the vapour cavity. Based on the experimental results, the evolution of the droplet and the cavity are influenced by two geometrical parameters: (1) the ratio of the cavity size to the droplet size and (2) the eccentricity of the cavity. The effects of these influencing factors on the displacement histories and time-varying lengths of the water droplet and the vapour cavity are discussed in this paper.

2. Experimental methods

Experiments are conducted in a horizontal shock tube with a length of 2.0 m for its test section, 0.9 m for its driven section, and 2.6 m for its driver section, as sketched in figure 1. The square cross section in the test section is 80 mm $\times$ 80 mm. A drop generator is mounted on top of the test section, and degassed distilled water is supplied to it. The flow field is visualized by direct high-speed photography, and a 150 W LED light source is utilized to provide diffusive light. The frame rate of the high-speed video camera is set to 50,000$\sim$80,000 f.p.s., and the spatial resolution of the image is 0.018 mm pixel^{-1}.

Before each experimental run, the air in the test section and the driven section is sucked away by a vacuum pump (Leybold DIVAC), and the final pressure is measured as $(5.3\pm0.5)\times10^3$ Pa with a vacuum pressure gauge (SMC GZ46-K2K). First, a signal generator is employed to trigger both the high-speed camera (FASTCAM SA-Z, Photron Limited) and the delay generator (DG535). Then, the delay generator provides a signal with an adjustable time delay to the electromagnetic valves of the drop generator and the gas supply tank. Subsequently, the water droplets are formed periodically by the drop generator and fall into the test section. Meanwhile, the air inside the gas supply tank rushes into the driver section and bursts the diaphragm. Consequently, a shock wave moves towards the test section and interacts with the droplets.

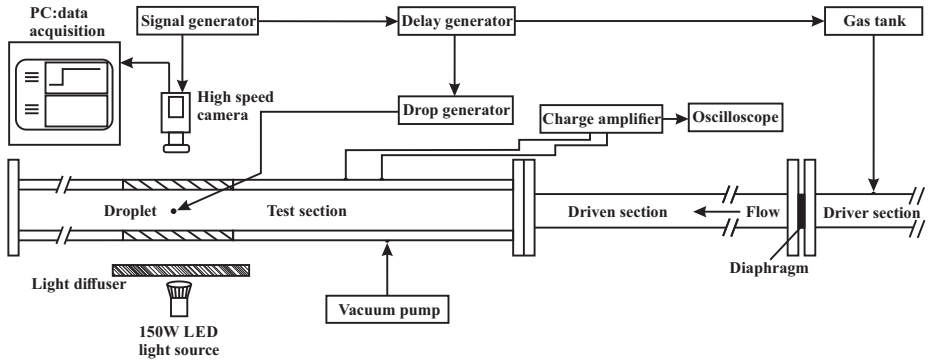

FIGURE 1. A schematic of the shock tube and instrumentation layout (top view).

Due to the heating effect of the LED light source, the temperature in the test section gradually rises to 34 °C, which is higher than the laboratory temperature (23 °C). Therefore, the surrounding pressure inside the test section reaches the saturation pressure of water (5.3×10^3 Pa) at 34 °C, and equilibrium between the liquid phase and gas phase is achieved. The vapour cavity is separated from the liquid but remains within the droplet. During a specific experimental run, the sizes of the droplet and vapour cavity and the position of the vapour cavity relative to the droplet cannot be controlled. The diameter of the droplet (D_d) varies from 1.14 mm to 3.04 mm, and that of the vapour cavity (D_c) varies from 0.68 mm to 2.71 mm. The incident shock Mach number measured by two piezoelectric transducers is 2.25±0.15. Reynolds numbers and Weber numbers of flows under different working conditions are also calculated by the following definitions:

$$Re = \frac{\rho_g U_{flow} D_d}{\mu_g}, \quad We = \frac{\rho_g U_{flow}^2 D_d}{\sigma} \tag{2.1}$$

where ρ_g, μ_g, and U_{flow} are the density, viscosity, and flow velocity of the post-shock gas, D_d denotes the diameter of droplet, and σ is the surface tension coefficient of water at the pre-shock temperature 34 °C. Here, another dimensionless parameter $We^*{=}p_g D_d/\sigma$ is also defined to compare the post-shock gas pressure p_g and the Laplace pressure. Geometrical and flow parameters in different cases are summarized in table 1. By using the relations of normal shock, We^* can be readily expressed in terms of shock Mach number M_s and traditional Weber number We:

$$\frac{We}{We^*} = \frac{4\gamma\left(M_s^2-1\right)^2}{\left[2\gamma M_s^2-(\gamma-1)\right]\left[2+(\gamma-1)M_s^2\right]} \tag{2.2}$$

where γ is the specific heat ratio of air. Since the shock Mach numbers of different cases are all about 2, the ratios of We to We^* are all 1.5 approximately in the present study.

3. Results and discussion

3.1. *Qualitative analysis*

Figure 2 shows experimental images of the hollow droplets in five representative cases (the corresponding movies to figure 2(a)-(e) are also attached). Time zero is defined as the instant at which the shock wave impacts the upstream wall of the droplet, and the time is normalized by D_d/U_{flow}. The upstream wall of the droplet (UW), the downstream wall of the droplet (DW), the upstream interface of the cavity (UI), and the downstream

Case No.	1	2	3	4	5	6	7	8	9
droplet diameter D_d (mm)	1.23	1.38	1.14	1.54	3.04	2.22	1.55	1.30	1.14
cavity diameter D_c (mm)	0.68	0.86	0.75	1.23	2.71	2.06	1.14	0.91	0.68
diameter ratio δ=D_c/D_d	0.55	0.62	0.66	0.80	0.89	0.92	0.74	0.70	0.59
eccentric distance S (mm)	0.06	-0.03	0.00	0.06	0.03	-0.03	-0.12	0.11	0.20
eccentricity ϵ=$S/(D_d/2)$	0.10	-0.04	0.00	0.08	0.02	-0.02	-0.15	0.17	0.34
U_{flow} (m/s)	457.8	577.0	480.6	480.6	481.6	456.0	511.7	512.0	510.0
Mach number	2.08	2.43	2.15	2.15	2.15	2.08	2.24	2.24	2.23
Reynolds number	3372	5002	3261	4419	8747	6048	4873	4063	3556
Weber number	618	1278	649	880	1745	1103	1051	877	764
We^*=$p_g D_d/\sigma$	455	700	449	609	1202	820	669	558	488

TABLE 1. The initial physical parameters in all cases. S represents the eccentric distance between the cavity center and the droplet center, and a positive or negative value indicates whether the cavity center is closer to the upstream or downstream wall of the droplet, respectively. U_{flow} and p_g represents the post-shock flow speed and pressure in the surrounding gas. σ is the surface tension coefficient of water.

interface of the cavity (DI) are all marked in figure 2(a). Note that the incident shock wave propagates from right to left in each image.

Case 5 has the largest average droplet diameter of 3.04 mm; therefore, the best image resolution is used as an example to describe the entire interaction process, as shown in figure 2(c). During the interaction of the incident shock wave and the droplet embedded with a vapour cavity (dimensionless time from 0 to 0.6), the external shape of the droplet remains almost undisturbed. However, the UI of the vapour cavity moves downstream slightly because the transmitted shock wave and the compression waves reflected from the UW impact on the UI repeatedly.

From dimensionless time 0.6 to 26.0, the DW becomes flattened and moves upstream because the DW is driven by the pressure difference between the high pressure generated by the shock-shock interaction behind the droplet and the low pressure generated by rarefaction waves inside the liquid. This observation is similar to the results of Xiang & Wang (2017); Meng & Colonius (2018) and Guan *et al.* (2018). In addition, the cavity shrinks substantially. In this process, local condensation of vapour can take place (Wu *et al.* 2019) because the local pressure inside the cavity can be higher than the saturation pressure after repeated impacts of shock/compression waves. In addition, a ring-like structure emerges on the outside surface of the droplet.

In the third frame of figure 2(c) for a dimensionless time of 29.2, a transverse jet is clearly observed along the symmetric axis of the droplet. Two explanations are given on the formations of the transverse jet. The first explanation is based on the Richtmyer-Meshkov instability (Richtmyer 1960; Meshkov 1969). As the Richtmyer-Meshkov instability (RMI) develops on the liquid-gas interface (UI) with an extreme Atwood number (Apazidis 2016), vorticity deposited by the misalignment between pressure gradient and density gradient drives the UI to penetrate into the vapour cavity (Xiang & Wang 2017). The second explanation emphasizes the mechanism that after the transmitted shock inside the droplet impacts the vapour cavity, rarefaction waves reflected from the vapour cavity relax the pressure near the UI, and the resultant temporal pressure gradient accelerates the flow in the streamwise direction. Due to the curved shape of UI, this acceleration focuses the flow to one point, eventually causing the flow to evolve and form the transverse jet (Hawker & Ventikos 2012). The mean velocity of the transverse jet in case 5 is measured by comparing the positions of the jet tip between two sequential images and

calculated to be V_{jet}=21.9±1.9 m/s. Here, V_{jet} is decomposed into three parts. The first part is the post-shock velocity of the interface UI, denoted by V_0. Based on the experimental images at the early stage of evolution, V_0 is evaluated to be 4.73 m/s. The second part is the RMI growth rate V_{RMI} of interface UI, which equals 6.69 m/s. This rate is calculated by the impulsive theory (Richtmyer 1960):

$$V_{RMI} = kaAV_0 \tag{3.1}$$

where k=$\sqrt{2}/a$ is the wave number (Haas & Sturtevant 1987), a is the cavity radius, and A=1 is the Atwood number. The rest (approximately 10.48 m/s) is the velocity induced by other mechanisms, such as the flow penetration due to the reflected rarefaction waves and the effect of cavity collapse.

When the transverse jet impacts DI with a large momentum, a great temperature rise is produced at the impact point (Bourne & Field 1992; Hawker & Ventikos 2012). Therefore, the vapour cavity expands, accompanied by local evaporation. As the volume of the vapour cavity increases, the DI catches up with the DW. Later, a water jet is observed at the downstream pole of the droplet (dimensionless time 57.7). To the best of the authors' knowledge, this water jet has not been observed in previous experimental studies on the shock-droplet interaction. Eventually, the water jet is covered by the fine mist generated by the droplet breakup at dimensionless time 86.2.

Other interesting findings include the effects of the cavity size and position on droplet deformation. When the ratio of the cavity diameter to the droplet diameter δ is sufficiently large (figure 2(c)), a mushroom-like vortex ring appears on the head of the water jet because of the Kelvin-Helmholtz instability induced by the velocity shear, and the surface of the UW is prominently rippled, which is different from the smooth liquid surface in the classical shock-droplet interaction experiments (Theofanous & Li 2008). The eccentricity of the vapour cavity ϵ also influences the droplet deformation. When the cavity is closer to the downstream wall, the water jet is long and thin, as shown in figure 2(d). When the cavity is closer to the upstream wall, the water jet is short and thick, as shown in figure 2(e).

In summary, droplet deformation is significantly influenced by cavity evolution, and cavity evolution can be divided into two stages: a cavity-collapse stage and a cavity-expansion stage. The entire flow process is governed by multiple physical mechanisms, including shock/rarefaction wave dynamics, interface instabilities, and gas-liquid phase changes.

3.2. *Droplet evolution*

The time-varying displacements of the upstream wall boundaries (UWBs) and the downstream wall boundaries (DWBs) in different cases are shown in figure 3. The dimensionless displacement is defined as (x_d-x_{0d})/D_d, where x_d is the displacement of the UWB or DWB and x_{0d} is the initial position of the UWB. For all cases, after the incident shock wave impacts on the hollow droplet, the UWB displacement (triangle symbol) increases gradually with a positive acceleration because of the accelerating effect of the rarefaction wave reflected from the DW. Moreover, the displacement of the DWB (square symbol) decreases slightly at first and then increases because the DI is pushed downstream by both the transverse jet impingement and the local evaporation of water.

In figure 3(a), when the eccentricity is sufficiently small (|ϵ|<=0.1), the time-varying displacements of the UWBs for different δ values almost coincide, which indicates that δ has little influence on the motion of the UW. In addition, the movement of the DWB increases when δ is larger. In the subfigure of figure 3(a), the dimensionless time is redefined as $tU_{flow}D_c/D_d^2 = (tU_{flow}/D_d)\delta$. The time-varying displacements of the DWBs

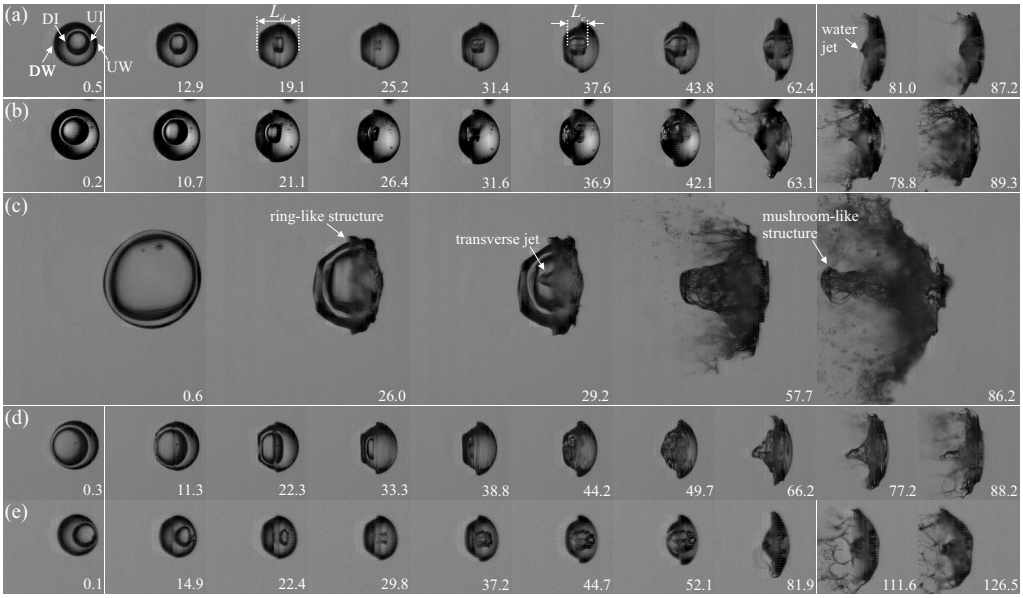

FIGURE 2. Evolution of the droplet embedded with a vapour cavity under the impact of a planar shock wave in different experimental cases. Subfigures (a), (b), (c), (d), and (e) correspond to cases 1, 2, 5, 7, and 9 in table 1, respectively. The incident shock wave travels from right to left. UW and DW denote the upstream wall and the downstream wall of the droplet, respectively. UI and DI denote the upstream interface and the downstream interface of the vapour cavity, respectively. L_d and L_c are the streamwise lengths of the droplet and the cavity, respectively. The dimensionless time tU_{flow}/D_d is shown in each image.

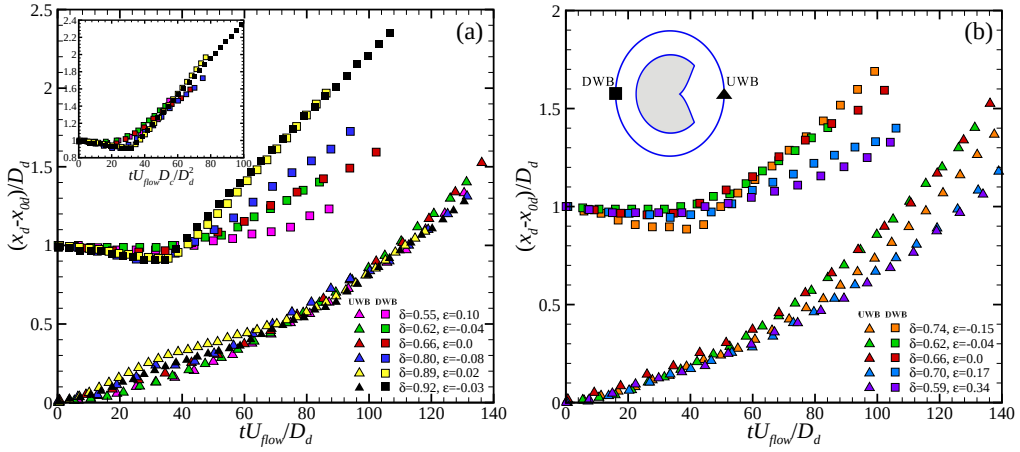

FIGURE 3. The comparison of the dimensionless displacements on the characteristic points of the droplets for different cases: (a) different δ and small ϵ ($|\epsilon|\leqslant 0.1$); (b) different ϵ and similar δ ($0.59\leqslant\delta\leqslant 0.74$). Triangle symbols and square symbols represent the UWB displacements and the DWB displacements obtained from the experimental images, respectively.

almost coincide with this new dimensionless method, which means that the water jet velocity is nearly proportional to δ.

In figure 3(b), when δ varies over a small range ($0.59\leqslant\delta\leqslant 0.74$), the time-varying displacements of the UWBs in the cases with the negative ϵ ($\leqslant$-0.1) are smaller than those in the cases with $\epsilon\sim 0$, while those in the cases with positive ϵ ($\geqslant 0.1$) reduce even more.

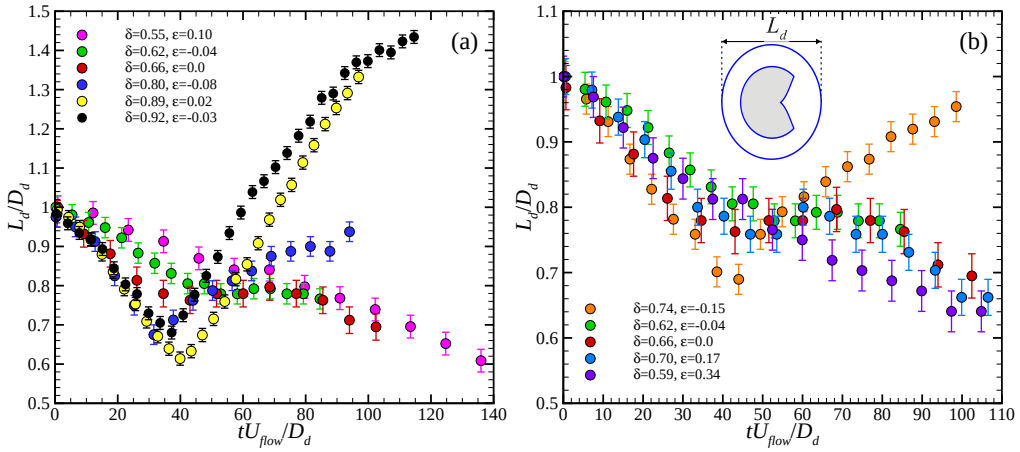

FIGURE 4. The comparison of the dimensionless streamwise lengths of the droplets for different cases: (a) different δ and small ϵ ($|\epsilon|\leqslant 0.1$); (b) different ϵ and similar δ ($0.59\leqslant\delta\leqslant 0.74$).

Therefore, when the vapour cavity center is misaligned with the droplet center, the vapour cavity impedes the motion of the UW, especially when the vapour cavity is closer to the UW. In addition, the time-varying displacement of the DWB with negative ϵ ($\leqslant$-0.1) is similar to those in the cases with $\epsilon\sim 0$, but those in the cases with positive ϵ ($\geqslant 0.1$) are smaller. In general, as ϵ increases, the time-varying displacement of the DWB decreases.

The time-varying lengths of the droplets (L_d) in different cases are shown in figure 4. The time is normalized as tU_{flow}/D_d, and the length is normalized as L_d/D_d. Figure 4(a) demonstrates the comparison between cases with sufficiently small eccentricity ($|\epsilon|<=0.1$) and different values of δ. When $\delta\geqslant 0.8$, L_d first decreases and then increases because the water jet velocity is larger than the velocity of the UWB. However, when $\delta\leqslant 0.66$, due to the limited momentum of the transverse jet, the induced velocity of the water jet is larger than the velocity of the UWB only during a short period. Consequently, L_d first decreases, then increases slightly, and finally decreases again during the observation time. In figure 4(b), δ varies within a small range ($0.59\leqslant\delta\leqslant 0.74$), but ϵ varies significantly. When ϵ=-0.15, L_d first decreases and then increases. However, for the cases with $\epsilon\geqslant$-0.04, L_d first decreases, then increases for a short period, and finally decreases again. In summary, when the size of the cavity is relatively large or the position of the cavity is closer to the downstream wall, the water jet is faster, and thus the length of the droplet is longer.

3.3. *Cavity evolution*

The time-varying displacements of the upstream interface boundaries (UIBs) and the downstream interface boundaries (DIBs) in different cases are shown in figure 5(a). The normalized displacement is defined as $(x_c\text{-}x_{0c})/D_c$, where x_c is the displacement of the UIB or DIB and x_{0c} is the initial position of the UIB. After the transmitted shock wave passes through the vapour cavity, the UI moves downstream as a result of the shock impact and the cavity collapse. Meanwhile, the DI moves upstream because of the high pressure generated by the shock-shock interaction near the downstream pole of the cavity as well as the cavity collapse. Before the vapour cavity shrinks to a tiny core, the transverse jet inside the cavity impacts the DI, and the volume of cavity is minimized at this time point. Thereafter, the DI is pushed downstream, and the UI is driven upstream because of the momentum exchange between the transverse jet and DI and the local

evaporation of water, which expands the vapour cavity. The time-varying displacements of the UIBs and DIBs in almost all the cases show agreement in their variation trends.

The time-varying lengths of the vapour cavity (L_c) in different cases are shown in figure 5(b). The normalized length is defined as L_c/D_c. In general, both δ and ϵ have limited influences on the evolution in the vapour cavity size. The decrease in L_c corresponds to the cavity-collapse stage, which is caused by shock compression and possibly vapour condensation. The subsequent increase in L_c corresponds to the cavity-expansion stage, which is ascribed to the transverse jet impingement and the water evaporation.

A theoretical estimation of the time-varying cavity length can be obtained by solving a simplified cavity collapsing problem, which is assumed to be of spherical symmetry as sketched in figure 6(a). The evolution in the cavity radius $a(t)$ can be described by extending the Rayleigh-Plesset equation (Brennen 1995) to the scenario as shown in figure 6(a). In the modified Rayleigh-Plesset equation

$$\left(a-\frac{a^2}{R}\right)\frac{\mathrm{d}^2a}{\mathrm{d}t^2}+\left[\frac{3}{2}-2\left(\frac{a}{R}\right)+\frac{1}{2}\left(\frac{a}{R}\right)^4\right]\left(\frac{\mathrm{d}a}{\mathrm{d}t}\right)^2=\frac{p_{sat}-p_\infty}{\rho} \tag{3.2}$$

ρ denotes the density of water, p_{sat} is the saturation pressure of water at the experimental temperature, and the surrounding pressure p_∞ is assumed to be the post-shock air pressure. The droplet radius $R(t)$ is related to the cavity radius $a(t)$ by the continuity of liquid:

$$R^3(t)=a^3(t)+R_0^3-a_0^3 \tag{3.3}$$

The derivation of equations (3.2) and (3.3) is provided in Appendix A. In the limit of $R\to\infty$, equation (3.2) reduces to the classical Rayleigh-Plesset equation for a vapour bubble in an infinite volume of liquid. A limitation of the present modelling comes from the assumption of undisturbed vapour pressure p_{sat}. In the future work, effects of thermodynamics and heat transfer on the evaluation of p_{sat} need to be incorporated into the collapse dynamics.

With initial conditions and physical parameters in accordance with those in experimental case 6, the above equations are numerically solved, and the collapsing history of the vapour cavity is plotted in figure 6(b). The comparison between the theoretical results and corresponding experimental data indicates that the idealized theoretical model in bubble dynamics still provides a good estimation of the time-varying cavity length, even though the present problem involves complex flow physics. For a vapour cavity in an infinite volume of water with initial radius a_0, the total collapse time has the following theoretical expression, known as the Rayleigh time (Lord Rayleigh 1917; Brennen 1995):

$$\tau_R=\sqrt{\frac{3\pi}{2}}\frac{\Gamma(5/6)}{\Gamma(1/3)}a_0\sqrt{\frac{\rho}{p_\infty-p_{sat}}} \tag{3.4}$$

where Γ is the Gamma function. Based on the parameters in case 6, the normalized Rayleigh time $\tau_R U_{flow}/D_d$ is equal to 42.62, which overestimates the collapse time, in comparison with the results in figure 6(b). Therefore, it is necessary to consider the effect of finite droplet size in modelling the collapse dynamics for the present problem.

4. Conclusions

A series of shock-tube experiments on the interaction of a planar shock wave and a water droplet embedded with a vapour cavity are performed to investigate the evolution of both the droplet and the cavity. Droplets with cavities of different sizes and eccentricities are generated by depressurizing the surrounding air, and equilibrium between the liquid

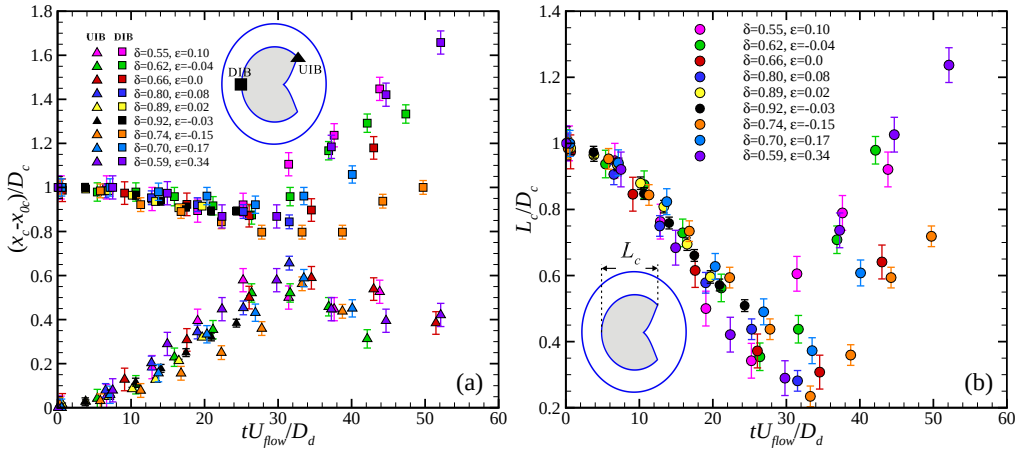

FIGURE 5. (a) Comparison of the dimensionless displacements of the UIBs and DIBs for different cases. Triangle symbols and square symbols represent the UIB displacements and the DIB displacements obtained from the experimental images, respectively. (b) Comparison of the dimensionless lengths of cavities for all cases.

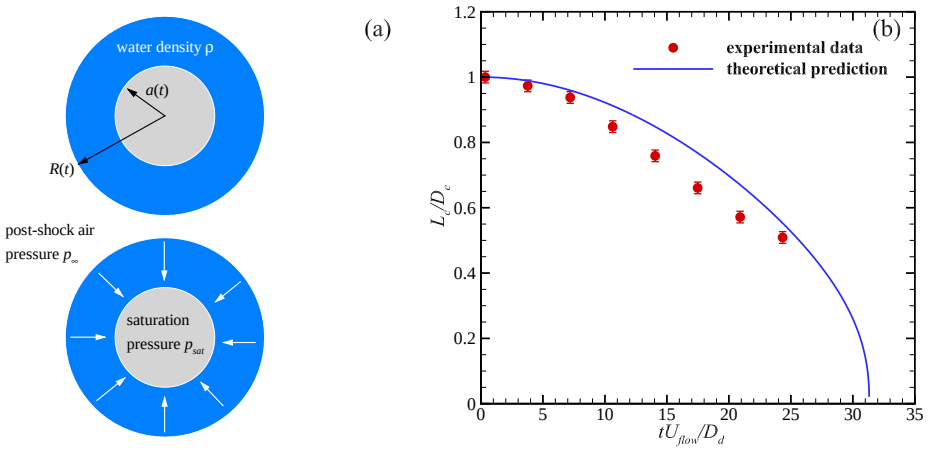

FIGURE 6. (a) Schematics of a spherical collapsing model for a water droplet embedded with a vapour cavity. The droplet is immersed in uniform air with a pressure equal to the post-shock air pressure in the present experiment. The pressure inside the cavity is assumed to be the saturation pressure of water. (b) Theoretical prediction and experimental data for the time-varying cavity size in the collapsing stage of case 6.

phase and the gas phase inside each droplet is obtained. Direct high-speed photography is adopted to capture the clear experimental images. Both the droplet outlines and the vapour cavity profiles are identified.

Compared with regular shock-droplet interactions, the physical process observed in the present work demonstrates different characteristics. The evolution of the vapour cavity obviously influences the deformation of the outside surface of the droplet. According to the time variation in the cavity volume, the evolution of the cavity can be divided into a cavity-collapse stage and a cavity-expansion stage. In the cavity-collapse stage, a transverse jet emerges from the upstream interface and impacts on the downstream interface. As a result of the transverse jet impingement, a water jet appears at the downstream pole of the droplet during the cavity-expansion stage.

The effects of the relative size and eccentricity of the cavity on the movement and deformation of the hollow droplet are analysed quantitatively. When the size of the cavity is relatively large or the position of the cavity is closer to the downstream wall, the water jet is faster, and thus, the length of the droplet is longer. However, these factors have limited influences on the cavity evolution. A suitable estimation of the cavity collapsing history can be provided by solving the modified Rayleigh-Plesset equation.

The interaction of a shock wave and a liquid droplet embedded with a vapour cavity poses a great challenge for the numerical simulation method, considering the complex wave system, unstable liquid-gas interfaces, and the possible phase change process. Therefore, the present experiments provide valuable benchmarks for numerical solvers aimed at compressible two-phase flows. The present experimental data and images can serve as reference results for numerical validation purposes. Future works will include developing numerical methods for multi-phase flows with viable phase-change models and numerical studies of shock-droplet interactions considering vapour cavities inside the droplets.

This work was supported by the Natural Science Foundation of China (grant no. 11772284) and Research Grants Council of Hong Kong (grant no. GRF 152151/16E).

Declaration of Interests. None.

Appendix A

This appendix outlines the derivation of the modified Rayleigh-Plesset equation, which describes the cavity evolution inside the droplet as sketched in figure 6(a). The flow field is assumed to be of spherical symmetry. By ignoring the change in liquid density ρ, the continuity equation for the liquid phase can be expressed in spherical coordinates as

$$\frac{1}{r^2}\frac{\partial\left(r^2u\right)}{\partial r}=0 \tag{A 1}$$

where the flow velocity $u(t,\,r)$ is in the radial direction. From equation (A 1) and the boundary condition for velocity at the liquid-vapour interface (r=a):

$$u(t,a)=\frac{\mathrm{d}a}{\mathrm{d}t} \tag{A 2}$$

the velocity field can be derived and expressed in term of the cavity radius $a(t)$ as

$$u(t,r)=\frac{\mathrm{d}a}{\mathrm{d}t}\frac{a^2(t)}{r^2} \tag{A 3}$$

The velocity at r=R is equal to the change rate of the droplet radius, thus

$$\frac{\mathrm{d}R}{\mathrm{d}t}=u(t,R)=\frac{\mathrm{d}a}{\mathrm{d}t}\frac{a^2(t)}{R^2(t)} \tag{A 4}$$

Integrating equation (A 4) yields

$$R^3(t)=a^3(t)+R_0^3-a_0^3 \tag{A 5}$$

where R_0 and a_0 are the radii of droplet and cavity at t=0, respectively.

By ignoring the viscous force, the surface tension, and the gravity, the momentum equation for the liquid phase can be written in spherical coordinates as

$$\frac{\partial u}{\partial t}+u\frac{\partial u}{\partial r}=-\frac{1}{\rho}\frac{\partial p}{\partial r} \tag{A 6}$$

Assume that the droplet is immersed in a uniform gas with a pressure p_∞ and the cavity

is filled with a saturated water vapour which has a pressure p_{sat}. Then, integrating equation (A 6) with respect to r, we obtain

$$\int_{a(t)}^{R(t)} \left(\frac{\partial u}{\partial t} + u \frac{\partial u}{\partial r} \right) \mathrm{d}r = \frac{p_{sat} - p_\infty}{\rho} \tag{A 7}$$

After substituting equation (A 3) into equation (A 7) and performing the integration, the resulting equation is

$$\left(a - \frac{a^2}{R} \right) \frac{\mathrm{d}^2 a}{\mathrm{d}t^2} + \left[\frac{3}{2} - 2 \left(\frac{a}{R} \right) + \frac{1}{2} \left(\frac{a}{R} \right)^4 \right] \left(\frac{\mathrm{d}a}{\mathrm{d}t} \right)^2 = \frac{p_{sat} - p_\infty}{\rho} \tag{A 8}$$

where the relation between $R(t)$ and $a(t)$ are provided by equation (A 5).

REFERENCES

Apazidis, N. 2016 Numerical investigation of shock induced bubble collapse in water. *Phys. Fluids* **28** (4), 046101.

Bhattacharya, S. 2016 Interfacial wave dynamics of a drop with an embedded bubble. *Phys. Rev. E* **93**, 023119.

Bourne, N. K. & Field, J. E. 1992 Shock-induced collapse of single cavities in liquids. *J. Fluid Mech.* **244**, 225–240.

Brennen, C. E. 1995 *Cavitation and Bubble Dynamics*, pp. 34–37. Oxford University Press.

Brujan, E. A., Keen, G. S., Vogel, A. & Blake, J. R. 2002 The final stage of the collapse of a cavitation bubble close to a rigid boundary. *Phys. Fluids* **14** (1), 85–92.

Field, J. E., Dear J. P. & Ogren, J. E. 1989 The effects of target compliance on liquid drop impact. *J. Appl. Phys.* **65** (2), 533–540.

Field, J. E., Camus, J. J., Tinguely, M., Obreschkow, D. & Farhat, M. 2012 Cavitation in impacted drops and jets and the effect on erosion damage thresholds. *Wear* **290**, 154–160.

Guan, B., Liu, Y., Wen, C. Y. & Shen, H. 2018 Numerical study on liquid droplet internal flow under shock impact. *AIAA J.* **56** (9), 3382–3387.

Guildenbecher, D., López-Rivera, C. & Sojka, P 2009 Secondary atomization. *Exp. Fluids* **46** (3), 371–402.

Haas, J. F. & Sturtevant, B. 1987 Interaction of weak shock waves with cylindrical and spherical gas inhomogeneities. *J. Fluid Mech.* **181**, 41–76.

Hawker, N. A. & Ventikos, Y. 2012 Interaction of a strong shockwave with a gas bubble in a liquid medium: a numerical study. *J. Fluid Mech.* **701**, 59–97.

Joseph, D. D., Belanger, J. & Beavers, G.S. 1999 Breakup of a liquid drop suddenly exposed to a high-speed airstream. *Int. J. Multiphas. Flow* **25** (6), 1263–1303.

Kodama, T. & Tomita, Y. 2000 Cavitation bubble behavior and bubble–shock wave interaction near a gelatin surface as a study of in vivo bubble dynamics. *Appl. Phys. B* **70** (1), 139–149.

Kondo, T. & Ando, K. 2016 One-way-coupling simulation of cavitation accompanied by high-speed droplet impact. *Phys. Fluids* **28** (3), 033303.

Liu, L., Ma, W., Liu, Y. & Cui, J. 2018 Study on mechanism of bubble growth within a water droplet under rapid depressurization. *Int. J. Heat Mass Transf.* **119**, 709–719.

Lord Rayleigh, O. 1917 On the pressure developed in a liquid during the collapse of a spherical cavity. *Philos. Mag.* **34** (200), 94–98.

Meng, J. C. & Colonius, T. 2018 Numerical simulation of the aerobreakup of a water droplet. *J. Fluid Mech.* **835**, 1108–1135.

Meshkov, E. E. 1969 Instability of the interface of two gases accelerated by a shock wave. *Fluid Dyn.* **4**, 101–104.

Philipp, A. & Lauterborn, W. 1998 Cavitation erosion by single laser-produced bubbles. *J. Fluid Mech.* **361**, 75–116.

Richtmyer, R. D. 1960 Taylor instability in shock acceleration of compressible fluids. *Commun. Pure Appl. Math.* **13**, 297–319.

Sembian, S., Liverts, M., Tillmark, N. & Apazidis, N. 2016 Plane shock wave interaction with a cylindrical water column. *Phys. Fluids* **28** (5), 056102.

Shpak, O., Verweij, M., de Jong, N. & Versluis, M. 2016 *Droplets, Bubbles and Ultrasound Interactions*, pp. 157–174. Springer International Publishing.

Theofanous, T. G. 2011 Aerobreakup of newtonian and viscoelastic liquids. *Annu. Rev. Fluid Mech.* **43**, 661–690.

Theofanous, T. G. & Li, G. J. 2008 On the physics of aerobreakup. *Phys. Fluids* **20** (5), 052103.

Wierzba, A. & Takayama, K. 1988 Experimental investigation of the aerodynamic breakup of liquid drops. *AIAA J.* **26** (11), 1329–1335.

Wu, W., Wang, B. & Xiang, G. 2019 Impingement of high-speed cylindrical droplets embedded with an air/vapour cavity on a rigid wall: numerical analysis. *J. Fluid Mech.* **864**, 1058–1087.

Xiang, G. & Wang, B. 2017 Numerical study of a planar shock interacting with a cylindrical water column embedded with an air cavity. *J. Fluid Mech.* **825**, 825–852.